A. Dvornova, G. T. A. Huijsmans (ID), S. Sharapov, F. J. Artola Such (ID), P. Puglia, M. Hoelzl (ID), S. Pamela, A. Fasoli, and D. Testa

View Online　　**Export Citation**　　**CrossMark**

Modeling of TAE mode excitation with an antenna in realistic X-point geometry

View Online   Export Citation   CrossMark

A. Dvornova,[1,2,3] G. T. A. Huijsmans,[2,3] [ID] S. Sharapov,[4] F. J. Artola Such,[5] [ID] P. Puglia,[6] M. Hoelzl,[7] [ID] S. Pamela,[4]
A. Fasoli,[6] and D. Testa[6]

AFFILIATIONS

[1]Aix-Marseille Universite, CNRS, PIIM UMR 7345, 13397 Marseille, France
[2]Eindhoven University of Technology, 5612 AZ Eindhoven, The Netherlands
[3]CEA, IRFM, F-13108 Saint-Paul-lez-Durance, France
[4]CCFE, Culham Science Centre, OX14 3DB Abingdon, United Kingdom
[5]ITER Organization, Route de Vinon sur Verdon, 13067 St Paul Lez Durance Cedex, France
[6]EPFL, SPC, CH-1015 Lausanne, Switzerland
[7]Max-Planck-Institut fur Plasmaphysik, 85748 Garching, Germany

ABSTRACT

Experimentally, it is observed that Toroidal Alfvén Eigenmodes (TAEs) are difficult to excite with an external antenna when the plasma is in X-point geometry. Here, the effect of the X-point geometry on the efficiency of the TAE excitation with the external antenna is investigated. In the first part of this paper, the influence of the near-last closed flux surface layer from the core side on the damping of the TAE modes is calculated using the linear resistive eigenvalue MHD code CASTOR. The resistive damping is identified as the main cause of the TAE damping in the open gap in the Alfvén continuum. It is shown that one aspect of the difficulty of excitation of the TAE modes in X-point geometry is an increased damping from the region inside the separatrix. However, the increased damping with the plasma boundary approaching the separatrix is not general and depends on the density profile shape. The second part of this paper discusses the influence of the TAE behavior in the limiter and X-point geometries including the scrape-off layer (SOL) in the reduced MHD code JOREK. It is shown that the dominant effect on the damping of the original TAE mode observed in the limiter configuration is caused by the additional damping in the region of open field lines, i.e., the SOL.

I. INTRODUCTION

Fusion plasmas are characterized by the presence of high energy particles produced as a result of the fusion reactions, or generated by ion cyclotron resonance, and neutral beam heating. The high performance of fusion devices requires the confinement time of these particles to be long enough for them to be thermalized and transfer energy to the bulk plasma before escaping the core region. A number of issues related to the redistribution and loss of these suprathermal particles were discovered. In tokamaks, one of the issues is the excitation of global shear Alfvén modes with their discrete eigenfrequencies existing in the gaps of the Alfvén continuum. These modes bear a generic name of gap modes. They can be driven by the free energy contained in the pressure gradient of the fast particles via wave-particle interactions since their velocity can be comparable with the Alfvén velocity: $v \sim v_{Alfven} = B_{tor}/\sqrt{\mu_0 \rho}$, where B_{tor} is the toroidal magnetic field and ρ is the plasma mass density. Toroidal Alfvén

Eigenmodes (TAEs)[1] are the name of the modes located in the gap of continuum occurring due to the toroidicity, which causes the coupling of m and $m+1$ poloidal harmonics. Being global modes, TAEs can lead to fast particle redistribution in space at nearly constant energy and therefore affect fast particle confinement, reduce heating and current drive efficiency, cause damage to the first wall, and decrease the overall plasma performance. Therefore, a clear understanding of the Alfvén mode dynamics is required for a careful operation of a fusion reactor.

TAE studies in the presence of fast particles are complicated due to the fact that the fast particle drive of the mode is changing since TAEs can cause redistribution of the particles. In order to exclude the effect of the altering particle drive, the dynamics of the TAE modes can be investigated by launching electromagnetic waves by an external antenna and detecting the TAE response in the form of resonance peaks with the saddle and pickup coils measuring perturbed radial and

poloidal magnetic fields correspondingly with a synchronous detection technique.

The numerical results of the TAE excitation by an external antenna presented in this paper were motivated by the experimental observations on the JET tokamak, where excitation of TAE modes with an external antenna has been very successful.[2] There, the in-vessel saddle coils were used to drive an n = 1 perturbation as an excitation source for the TAEs. The driving current is typically ∼30 A and is chosen to be such that the magnetic field perturbations are of the order of $\delta B/B \sim 10^{-5}$, which is small enough to avoid magnetic configuration distortion and direct changes in the fast particle confinement.

In order to detect the TAE modes, the applied frequency of the antenna sweeps over the frequency position of the potential TAE gap until the mode is detected via magnetic diagnostics. As an initial guess for a TAE frequency, a rough estimate of $\omega_{TAE} = v_A/2qR$ can be made, where q is the safety factor and R is the major radius, and typically is ∼100 − 200 kHz. Once the mode has been detected, frequency sweeps are reduced from the range, which allows us to cover the whole

toroidicity-induced gap to a range following the TAE resonance full width. An example of the frequency sweep range transition can be seen in the top figure in Fig. 1 at t = 58 s for discharge #42870. Knowing the response over the full resonance width, the resonance frequency and the damping rates determined as the HWHM (half width at half maximum) of the resonant peak can be calculated [Fig. 1(bottom)]. A more detailed overview of the JET antennas used for the TAE excitation in the series of experiments used in this paper can be found in Ref. 3 and references therein.

The analysis of the detected TAE peaks is based on a fitting of the transfer function presented in detail in Ref. 4. The transfer function describes the amplitude of the output signal as a function of the frequency of the input signal,

$$H(i\omega) = \frac{Y(i\omega)}{X(i\omega)} = \frac{F\{y(t)\}}{F\{x(t)\}},$$

where $H(j\omega)$ is a transfer function, y(t) and x(t) are the output and input signals, and $F\{y(t)\}$ and $F\{x(t)\}$ denote the Fourier transform of the signals. In order to derive the transfer function for TAE
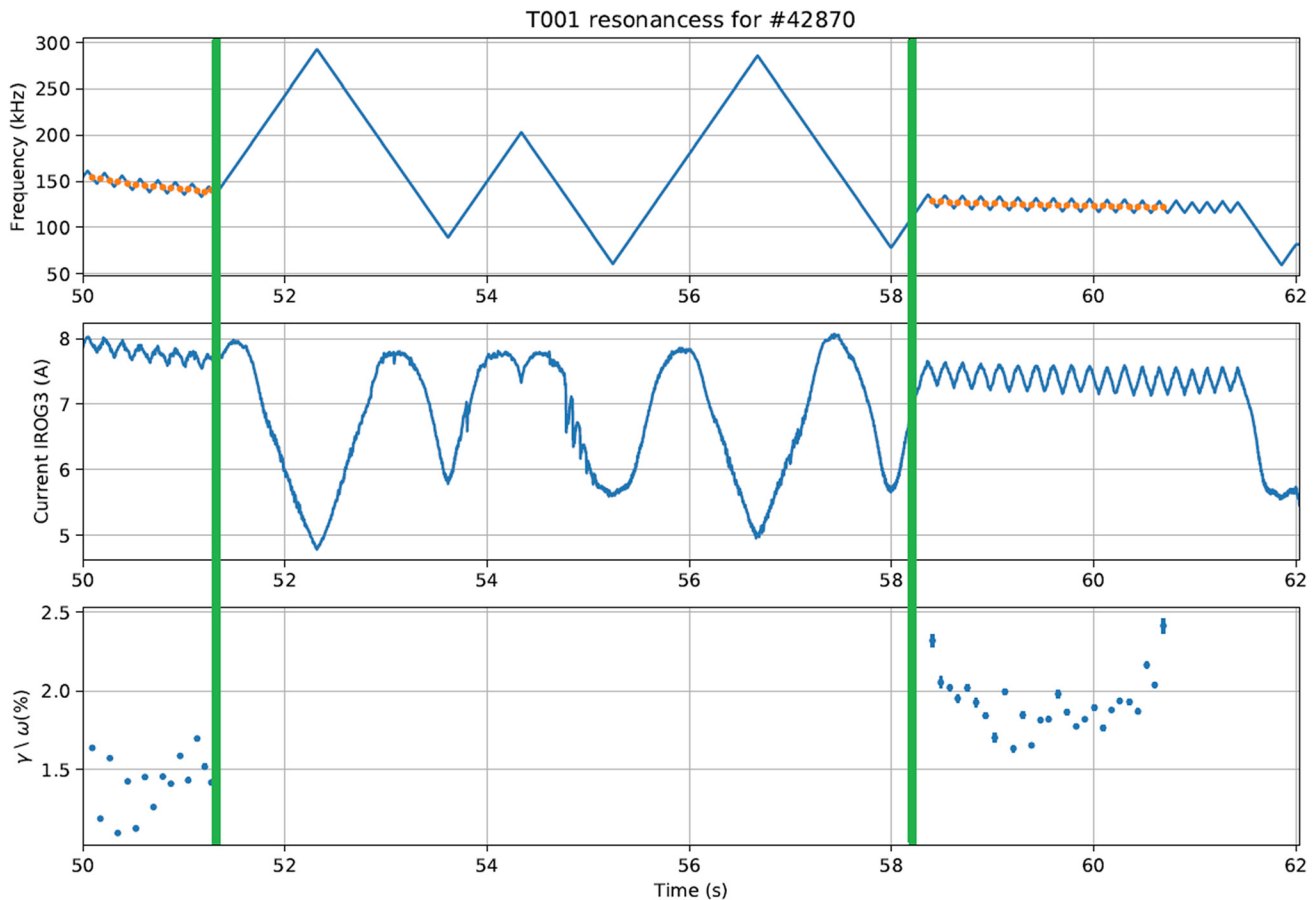
FIG. 1. Example of the experimental determination of the TAE resonance in the JET discharge #42870 with the external antenna being used as an active AE diagnostic as explained in Ref. 2. From top to bottom: (1) Blue line: the frequency of the externally applied perturbation as a function of time, orange line-tracked TAE frequency as a function of time. (2) Current in the pickup coils. (3) Relative damping rate of the TAE if it is detected. Note that the time interval 51.4 − 58.2 s corresponds to the X-point phase of the discharge, with the thick green vertical lines corresponding to the transition moment. The TAE mode could not be tracked in this interval of time.

detection, one simply needs to divide the output signal from diagnostics (such as pickup coils) by the input antenna current.

The presence of the Alfvén Eigenmodes means the existence of the poles in the derived transfer function so that it can be represented as

$$H(j\omega) = \sum_{k=1}^{N} \frac{1}{i\omega - p_k},$$

where N is the total number of resonances (corresponding to the total number of the TAEs in one gap), ω is the frequency of the input signal, and $p_k = \gamma_k + i\omega_{0k}$ is a pole describing the k-th resonance. Fitting the transfer function to all the available signals provides the values for ω_0—the TAE peak position, and γ—its damping rate in the absence of the fast particle drive. An example of such a fit for discharge #42870 is shown in Fig. 2, where orange lines correspond to the fitted function and blue lines correspond to the raw signal.

However, while TAEs excited with an antenna were clearly visible in the limiter phase of the discharge, they disappeared when the X-point formed in the magnetic configuration, possibly due to an increase in the damping rates.[5] This effect can be seen in Fig. 1. There, the TAE frequency of 150 kHz and a damping rate $\gamma/\omega \approx 1.5\%$ can be detected in the earlier stage of the discharge and disappear after the transition to an X-point configuration occurring at $t \approx 51.3$ s. Similarly, the TAE can again be detected after the transition back to the limiter configuration around $t \approx 58.2$ s. It has to be clarified that the TAEs exist in toroidal plasmas, independent of whether or not the driving source is present in the experiment, and the commonly used formulation of TAEs not existing simply means that the modes do not have a high enough amplitude to be detected by the magnetic diagnostics or cause a significant redistribution of particles.

The previous extensive studies (e.g., Refs. 6–9 and references therein) were performed to better understand the dynamics and damping mechanisms of global AE modes, showing that the damping rates increase significantly with shaping of the plasma and the gap between plasma and the external antenna, strongly depend on the variation of the plasma profiles at the edge, and are independent of the toroidal rotation shear.

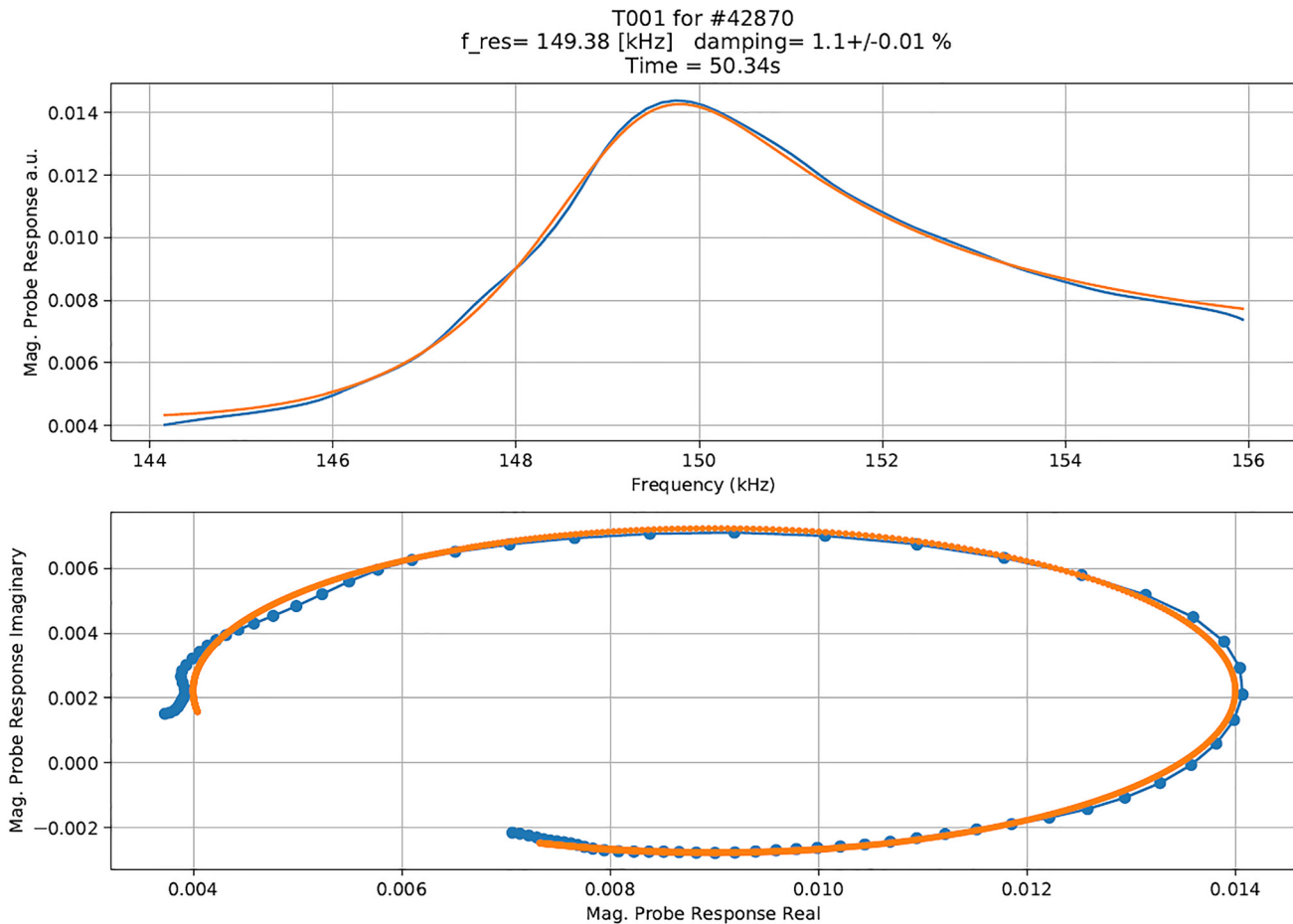**FIG. 2.** Example of the experimental determination of the TAE resonance in the JET discharge #42870 based on the technique discussed in Ref. 4. The technique is based on the fitting (solid orange lines) of the transfer function to the experimental magnetic data (blue dotted lines). The absolute value as a function of the antenna frequency (top) and the complex plane representation (bottom) of the pickup coil signal are illustrated.

The aim of the present work is to investigate in detail the effect of the X-point geometry on the efficiency of the TAE excitation with the external antenna and related damping rate. In the first study, the simplest viscoresistive fluid MHD model is assumed to suffice. It is clear that a further study should aim to include more possible (kinetic) damping mechanisms.[6] However, this is left for future work. In the first part of this paper, the influence of the near-LCFS (Last Closed Flux Surface) layer from the core side on the damping of the TAE modes is investigated using the linear resistive MHD code CASTOR.[10] The second part of this paper discusses the influence of the TAE behavior in the limiter and X-point geometries including the scrape-off layer (SOL) in the nonlinear reduced MHD code JOREK.[11] The code allows us to fully represent not only the core of the plasma but also the realistic geometry including the wall, the antenna, and the X-point with the SOL. The effects of the distance between the antenna and the width of the SOL on the TAE resonance behavior were studied.

II. DEPENDENCE OF THE DAMPING RATE ON THE NEAR-LCFS LAYER

A. Code description

In the first part of this paper, the behavior of the TAE in proximity of the separatrix with plasma's boundary approaching the separatrix from the core side is studied. Here, three codes are used in order to first reconstruct the equilibrium, then reconstruct the Alfvén continuum for a given equilibrium and density profile, and then calculate the plasma response to an external antenna signal. The electron density profile was measured in these discharges with the LIDAR diagnostics, while the ion mixture $n_T : n_D$ was measured by the relative intensity of T_α and D_α spectral lines of T and D atoms at the plasma edge, and also by Neutral Particle Analyzer and Active TAE diagnostics from the variation in v_A.[5] The EFIT code[12] was used in order to first reconstruct the experimental equilibrium. Further, the CSCAS[13] code was used for the calculation of the radial structure of the n = 1 Alfvén continuum determined for the given input density and equilibrium previously produced by EFIT. CSCAS is based on the model described in Refs. 14 and 15. In this model, an approximation of the dependence of the radial velocity and the magnetic field to be singular and logarithmic in nature is used according to.[16,17] This approximation is only correct for the ideal MHD model; therefore, plasma resistivity is not considered, and the resulting ideal continuum can only be used as a tool for finding an approximate TAE frequency and the location of the TAE gap. This is due to an effect known as the Alfvén paradox discussed in Ref. 18, where it is demonstrated that the resistive MHD continuum is not identical to the ideal MHD continuum even when $\eta \to 0$.

The analysis of the plasma response to the sweeping antenna signal was performed with the code CASTOR. The set of linearized resistive MHD equations solved by CASTOR is as follows:

$$\frac{\partial \rho_1}{\partial t} = -\nabla \cdot (\rho_0 \mathbf{v}_1),$$

$$\rho_0 \frac{\partial \mathbf{v}_1}{\partial t} l = -\nabla p_1 + (\nabla \times \mathbf{B}_0) \times (\nabla \times \mathbf{A}_1) + (\nabla \times \nabla \times \mathbf{A}_1) \times \mathbf{B}_0,$$

$$\rho_0 \frac{\partial T_1}{\partial t} l = -\rho_0 \mathbf{v}_1 \cdot \nabla T_0 - (\Gamma - 1)\rho_0 T_0 \nabla \cdot \mathbf{v}_1,$$

$$\frac{\partial \mathbf{A}_1}{\partial t} l = \mathbf{v}_1 \times \mathbf{B}_0 - \eta \nabla \times \nabla \times \mathbf{A}_1,$$

where ρ, p, $\mathbf{v}$, and T are the plasma mass density, pressure, fluid velocity, and temperature, $\mathbf{B}$ and $\mathbf{A}$ are the magnetic field and magnetic vector potential, η is the resistivity, and Γ is the specific heat ratio. The values with a subscript 0 denote the equilibrium quantities, and the ones with a subscript 1 denote the perturbations. Assuming that the variables evolve exponentially in time [as $a(\mathbf{r}, t) = a(\mathbf{r})e^{\lambda t}$], this system can be rewritten in a form of an eigenvalue problem as follows:

$$\mathbf{R} \cdot \mathbf{u} = \lambda \mathbf{S} \cdot \mathbf{u}, \qquad (1)$$

where $\mathbf{R}$ and $\mathbf{S}$ are the complex matrices and $\mathbf{u}$ is a vector of variables. The version of CASTOR used in this work[19] includes the external antenna, which works as a driving source of a given frequency ω_d. The system of equations can be represented instead of an eigenvalue problem in the following form:

$$(\mathbf{R} - i\omega_d \mathbf{S}) \cdot \mathbf{u} = \mathbf{a_d}(\omega_d), \qquad (2)$$

where $\mathbf{a_d}(\omega_d)$ is a driving term. This system provides a stationary state solution. With the drive frequency ω_d sweeping around the TAE frequency imitating the experiment, the radial structure, frequency, and damping rate of the TAE can be determined. In the code, the main plasma is surrounded by a vacuum and an ideally conducting wall. The antenna is situated inside the vacuum. In a resistive plasma, the boundary conditions for the tangential and normal components of the magnetic field are the so-called free-boundary conditions, i.e., continuity of the magnetic field across the plasma-vacuum interface. The continuity of the total pressure (kinetic and magnetic) implies that the pressure perturbation goes to zero at the boundary in a resistive plasma. The shape of the ideally conducting wall is taken to be the shape of the JET vacuum vessel.

B. Case setup

The equilibrium produced by the EFIT code from JET discharge #42870 discussed earlier was used in this work. For the analysis, two equilibria at $t = 52.3$ s and $t = 54.8$ s with the plasma in the X-point configuration were analyzed. Here, the plasma boundary is taken to be a closed field line flux surface approaching the separatrix. Both CASTOR and CSCAS can model shaped equilibria closely approaching the separatrix but cannot take into account the actual X-point due to the choice of the straight field line flux surface coordinate system.

The Alfvén continua for both equilibria taken at the times $t = 52.3$ s and $t = 54.8$ s were reconstructed using the CSCAS code, with the equilibria reconstructions corresponding to the X-point phase of the discharge at $t = 52.4$ s and $t = 54.8$ s are illustrated in Fig. 3. The toroidal rotation was not taken into account in the simulations as its effect is expected to be negligible in the purely Ohmic discharge. The Alfvén continuum with the q and normalized density profiles for the equilibria at $t = 54.8$ s are illustrated in Fig. 4. The experimental electron density in this moment was equal to $5 \times 10^{19} \text{m}^{-3}$. It can be seen that the TAE gap is closed due to an overlap with a continuum branch near the boundary. This means that the antenna signal of any frequency across the TAE gap will experience a strong continuum absorption when the propagating signal's frequency equals the local Alfvén frequency when crossing the continuum lines.

In order to exclude the effect of the continuum absorption, the original experimental density was varied in order to make the gap open to exclude the crossings and, therefore, the strong damping.
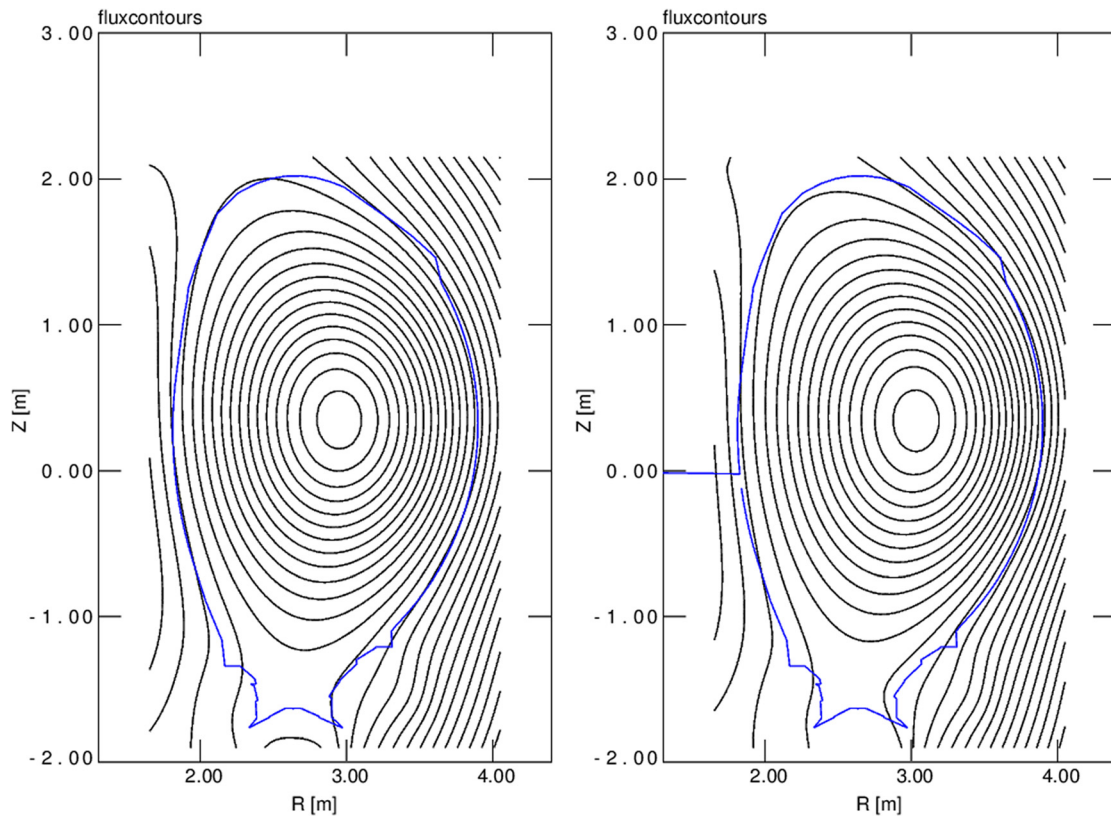
FIG. 3. Plasma equilibria reconstructed with the EFIT code for equilibria taken at t = 52.4 s (left) and t = 54.8 s (right). Black lines correspond to the flux surfaces and blue line to the real JET limiter.
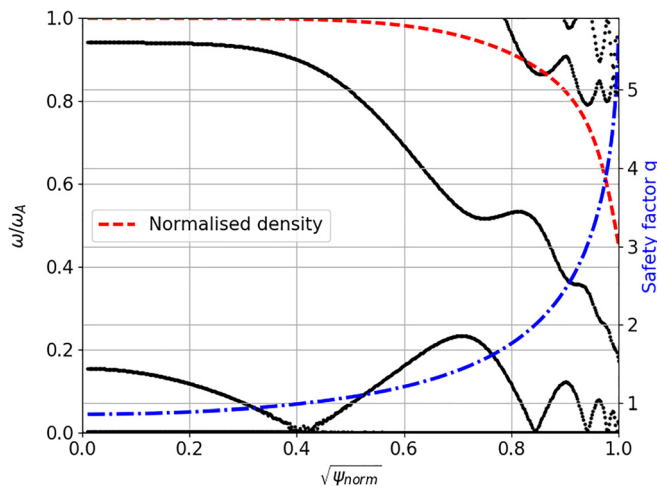

FIG. 4. Ideal n = 1 Alfvén continuum reconstructed with the CSCAS code for the equilibrium taken at t = 54.8 s, together with the corresponding experimental density (red dashed line) and q (blue dash-dotted line) profiles. The experimental density profile was obtained with the LIDAR diagnostics.

Here, the equilibrium at $t = 54.8$ s will be taken as an example. The original raw and fitted experimental density profiles are illustrated on the left in Fig. 5 in green, together with the corresponding Alfvén continua on the right in the same figure also in green. The experimental density profile was modified, and the two modified density profiles (corresponding to blue and red lines in the same plot) were chosen such that only the outer part of the continuum was changed, varying the width of the open TAE gap. While varying density, the equilibrium is kept constant, meaning that the pressure profile does not change, and the change of the density profile leads to a compensating change of the temperature profile. The uncertainty in the measured data allows such an assumption of a density variation in the pedestal region. The resulting Alfvén continua are on the right in Fig. 5 in red and blue, and an open gap in the normalized frequency range of $\omega/\omega_A \approx 0.23 - 0.4$ in the case in red and in the range $\omega/\omega_A \approx 0.23 - 0.47$ in the blue case is now present.

The sensitivity of the plasma response to the edge density profile is seen in Fig. 6 where the plasma response as a function of the applied antenna frequency is demonstrated with the use of the CASTOR code. It can be seen in the figure that the response corresponding to the original density profile (solid line) does not allow us to identify the TAE, whereas clear TAE peaks corresponding to two new density profiles are visible. According to Ref. 20, a possible effect of the TAE damping
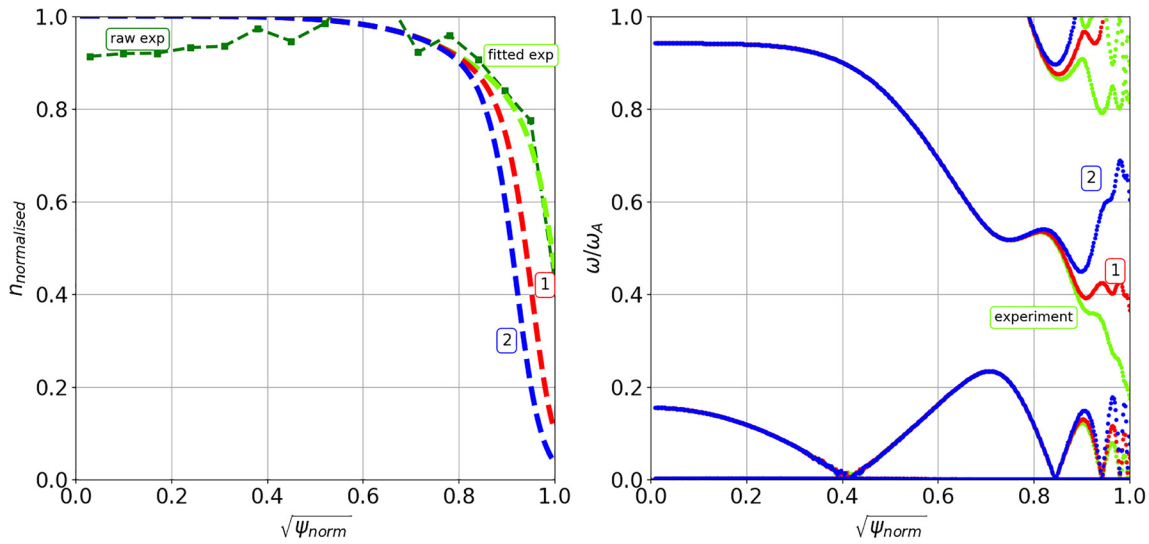
FIG. 5. (a) Raw and fitted experimental (in green, labeled "raw exp" and "fitted exp") and 2 modified, red (labeled "1") and blue (labeled "2"), density profiles for equilibrium taken at t = 54.8 s. (b) Ideal n = 1 Alfvén continua corresponding to the three different density profiles illustrated in (a). It can be seen that the experimental profile corresponds to the continuum with a closed TAE gap, therefore not allowing the TAE identification due to the strong continuum damping. Therefore, the modified density profiles were chosen in such a way that the TAE is less open (like in the case of the first modified profile) or more open (like in the case of the second modified profile).

induced in the open continuum gap in the proximity of the continuum tips can be taking place. Therefore, in this work, it was decided to study the sensitivity of the TAE peaks to the shape of the density in the edge. The two different modified density profiles with a lower density in proximity of the separatrix were chosen, leading to the different widths of the gaps.

One of the important parameters in the CASTOR code used here, which influences the TAE damping in the absence of the continuum damping,[16,21–23] is the plasma resistivity. It defines the resistive damping and, therefore, the width of the TAE peak, as illustrated in

Fig. 7. It can be seen that the damping approximately scales as $\approx \eta_{norm}^{1/2}$. For the following studies in this chapter, a realistic temperature-dependent Spitzer resistivity profile was used with the resistivity value of $\eta = 2.6 \times 10^{-8}$ Ωm, comparable to the experimental one of
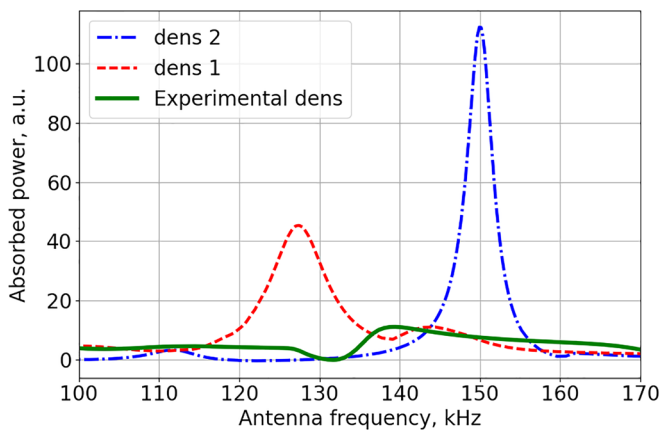

FIG. 6. Dependence of the power absorbed by the plasma calculated in the CASTOR code as a function of the applied antenna frequency for the three density input profiles shown in Fig. 5(a). The response function corresponding to the initial experimental density (in green solid line) shows that the TAE in this case is undetectable.
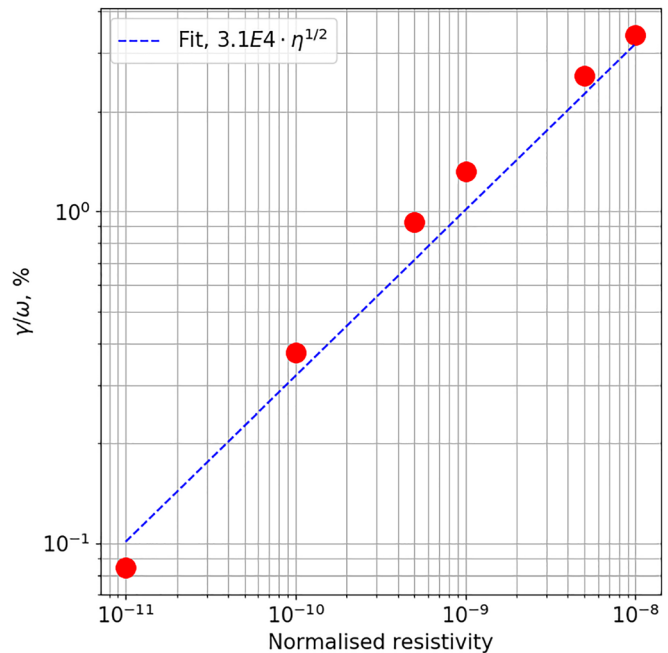

FIG. 7. Dependence of the power absorbed by plasma from sweeping antenna signal on the plasma resistivity. The increase in the damping as a function of plasma resistivity suggests the dissipative nature of the TAE damping in the absence of the continuum damping.
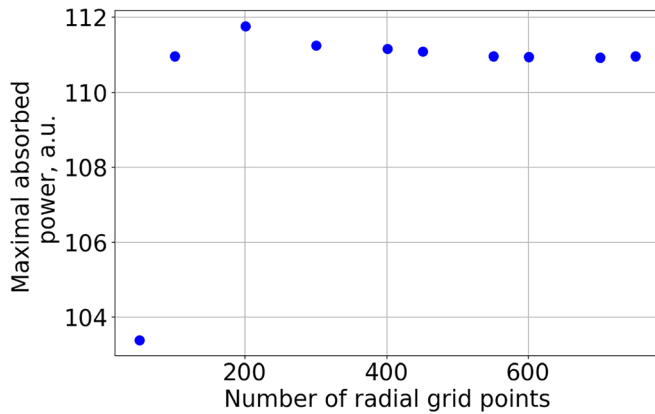
FIG. 8. Dependence of the amplitude of the TAE peak on the number of the grid points. The good convergence is achievable from the grid number of 601 points, which is used in the simulations.

$\eta \approx 5 \times 10^{-8}\,\Omega\text{m}$. A slightly lower value of the resistivity than the experimental one was chosen in order to avoid high damping. The plasma viscosity is not taken into account.

A study of the convergence of the damping rate/peak heights on the radial resolution of the grid (the number of points in the radial direction) was performed. As was discussed above, in ideal MHD sound and Alfvén waves, both cause singularities at the radial positions where the antenna frequency coincides with the local continuum frequency. The radial width of this singularity is determined by the strength of the damping mechanisms in plasma, therefore, resistivity in CASTOR. Therefore, the grid resolution in the simulations should be high enough to resolve the width of the near-singularity. The dependence of the maximal absorbed power (height of the TAE peak) on the grid resolution is shown in Fig. 8. Simulations presented hereafter are

performed with a radial resolution of 600 radial cubic finite elements that were sufficient in order to achieve a good convergence.

The goal of the presented work is to study the effect of the transition from the X-point to limiter configuration on the TAE stability/damping rate. For this purpose, the original equilibria was "cut" along a certain flux surface so that there are only closed flux surfaces present in the modeling domain. This maximal outermost flux surface taken into account (which will be called ψ_{max} in this work) can be chosen arbitrarily. Therefore, by varying $\psi_{\text{max}} = 0.95, \ldots, 0.995$ with $\psi_{\text{max}} = 1$ corresponding to a separatrix, it is possible to evaluate the change of the TAE damping rate with plasma simulation boundary approaching the separatrix.

For a fixed ψ_{max}, the simulation with the CASTOR code was performed by sweeping the frequency of the applied antenna signal, mimicking the experiment. As an example, let us consider an equilibrium at $t = 54.8$ s and the first density profile corresponding to the Alfvén continuum in Fig. 5 in red. The sweep across the open gap around $0.25 - 0.4\omega/\omega_A$ results in response functions corresponding to different fixed ψ_{max} as illustrated in Fig. 9(a). Two TAE response peaks can be identified: the first minor peak with a lower frequency at $f \approx 100$ kHz, and the second main peak with a higher frequency at $f \approx 130$ kHz. The corresponding damping rates of the two identified peaks calculated as HWHM are illustrated in Fig. 9(b). The damping rates of the first minor peak are not indicated for the $\psi_{\text{max}} = 0.99$, 0.995 as the damping rates are so high that the peak is not distinguishable. The main resonance at $f \approx 130$ kHz shows a damping rate similar to the experimental values of 1–2.5% in this discharge. The damping rate increases by a factor of three with the boundary approaching the separatrix, i.e., as $\psi_{\text{max}} \to 1$. Mode structures for both TAEs at $t = 54.8$ s are illustrated in Figs. 10 and 11, respectively.

It is worth mentioning that the Alfvén continua discussed before did not include sound waves with frequencies $\omega_S = k_\parallel \sqrt{\Gamma p/\rho}$. The inclusion of them is illustrated in Fig. 12 as a combination of Alfvén
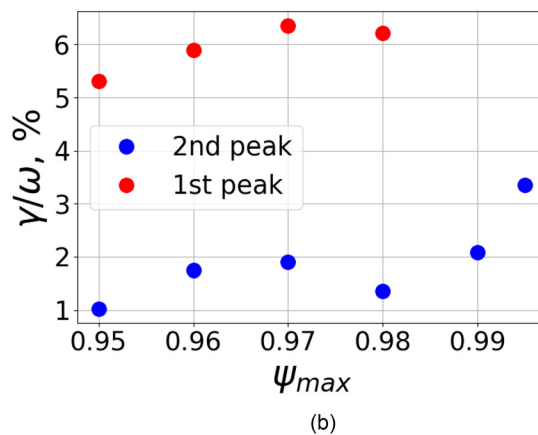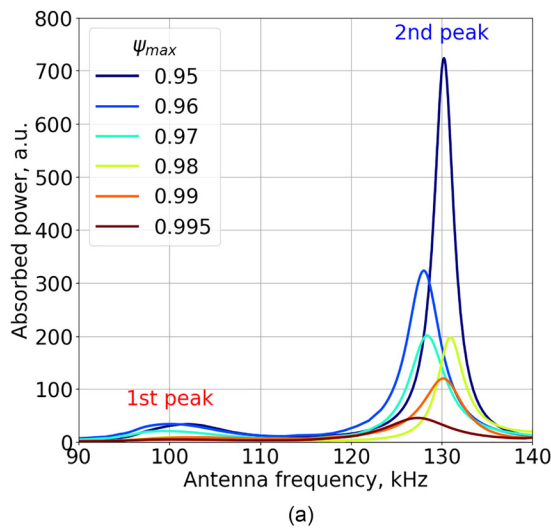

FIG. 9. Example of calculation of the (a) frequency scan, dependence of the power absorbed by the plasma as a function of the applied antenna signal, and (b) the damping rate, determined as the HFHM of the TAE response peak. Both are calculated for different normalized poloidal fluxes ψ_{max} at the boundary of the computational domain.
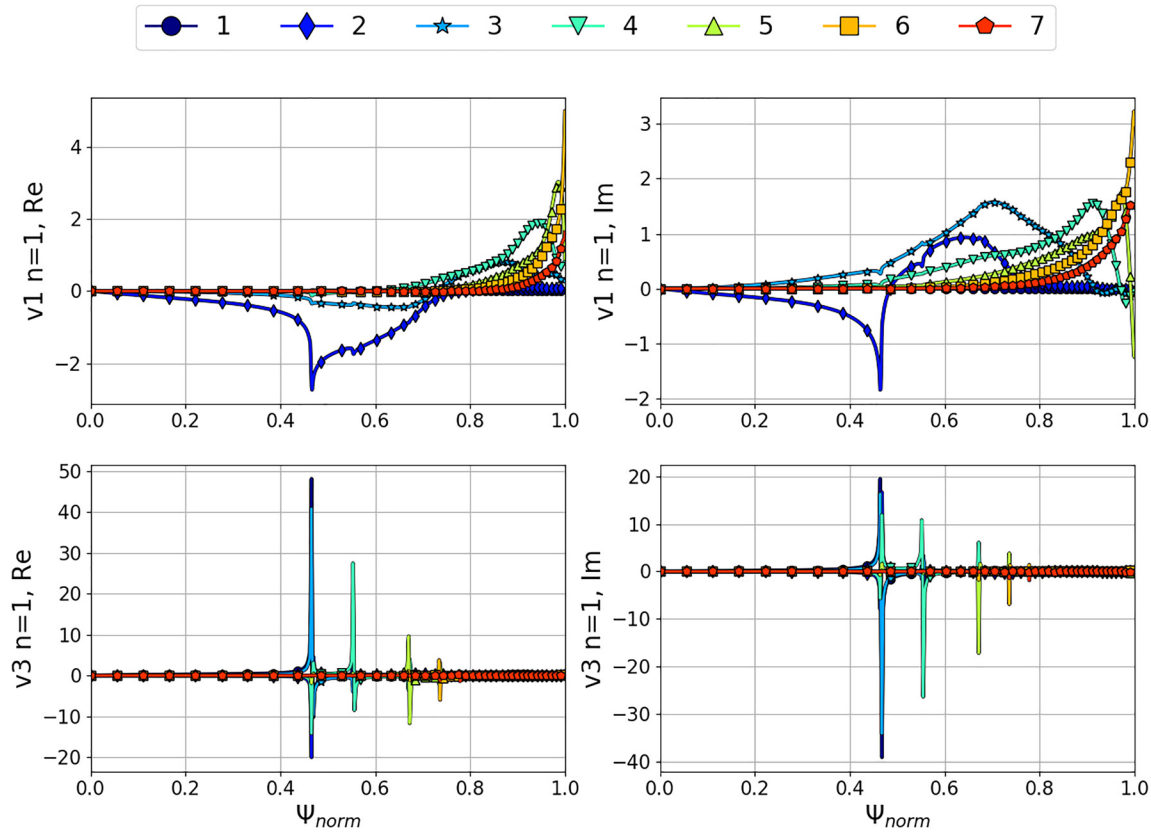
FIG. 10. Mode structure of the first $n = 1$ TAE peak for the equilibrium at $t = 54.8$ s corresponding to the lower resonant frequency. The top row shows the real and imaginary parts of the radial component of the velocity as a function of $s = \sqrt{\psi}$, bottom row—toroidal component of the velocity. Different symbols correspond to the different poloidal harmonics.

and sound continua in black in comparison with the same continua but only with the inclusion of the Alfvén waves in red. This will result in the overlap of the sound continuum with the toroidicity-induced open Alfvén gap leading to the change of the damping rate due to the absorption of the antenna wave energy by the sound wave at the locations where the antenna frequency matches the local sound wave frequency.

Sound waves were included in all the simulations described in this chapter. Their inclusion can be noticed if looking closely at the mode structure of the parallel velocity, where sharp singularities correlate with the crossings of the sound continuum discussed above. In comparison, the mode structures corresponding to the same case but with Γ set to zero are illustrated in Fig. 13. To determine the influence of the damping due to the sound waves, a set of simulations for the main TAE peak at $f \approx 130$ kHz without the inclusion of the sound waves were performed by setting $\Gamma = 0$. The results are demonstrated in Fig. 14. It can be seen in the figure that even though the sound waves have an influence on the damping rates, the difference does not change the global trend of the damping rate increase with an increase in ψ_{max}. The influence of the sound waves increases with the value of the poloidal beta, which in this case is $\beta_p = 0.74$, in agreement with the results demonstrated in Refs. 19 and 24. It should be mentioned

that for a high β_p value, a more sophisticated kinetic treatment is required.

Similar to the example above, for four cases total with both two equilibria and two density profiles, the frequency sweeps across the TAE gap range were performed, and in each case, two TAEs are identified. Only one TAE can be traced in the experiment, but it is likely that the dominant resonance with a higher frequency is measured.

The damping rates for the first TAE with a lower frequency and the second TAE peak with a higher frequency for all four cases are shown in Figs. 15 and 16, respectively. Overall, damping rates of 1%–3% of the main resonance are consistent with the experimental observations for the same discharge. It can also be seen in these figures that damping rates for the first density are overall higher for both TAE peaks in both equilibria due to the fact that the first density is higher at the edge, which leads to lower temperatures and higher resistivities, taking into account constant pressure. The effect is less pronounced for the lower frequency peak since it is localized closer to the core, and the change of resistivity in the edge does not influence it as much as the higher frequency peak. The sudden decrease in the damping rate for ψ_{max} increasing from 0.97 to 0.98 can be explained by the change of the q profile: the maximal value of q changes from $q = 4$ to $q = 5$; therefore, the mode structure and consequently the
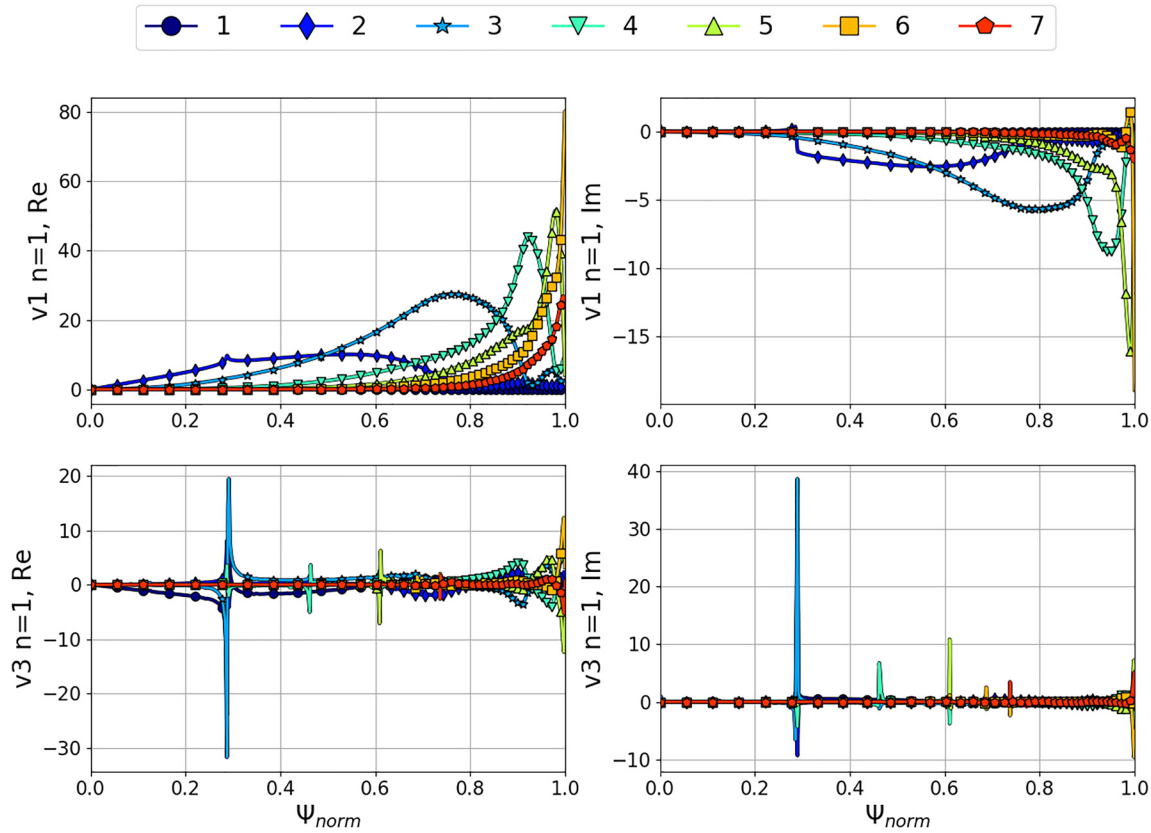
FIG. 11. Mode structure of the second n = 1 TAE peak for the equilibrium at t = 54.8 s corresponding to the higher resonant frequency. The top row shows the real and imaginary parts of the radial component of the velocity as a function of $s = \sqrt{\psi}$, bottom row—toroidal component of the velocity. Different symbols correspond to the different poloidal harmonics.

frequency change. As expected, the damping rate increases when approaching the separatrix. This result indicates that one aspect of the difficulty of excitation of the TAE modes in the X-point geometry is an increased damping from the region inside the separatrix. However, the

increased damping with the plasma boundary approaching the separatrix is not general and depends on the density profile shape.

III. TAE EXCITATION IN X-POINT GEOMETRY

Section II was concentrating on the change of the TAE behavior with the plasma boundary approaching the separatrix from the core side. In the second part of this paper, the causes of the TAE damping are studied in the JOREK code in the full X-point geometry.

A. Code description

The simulations were performed using the nonlinear MHD code JOREK. The MHD model used in this work is a single-fluid viscoresistive reduced MHD. The reduced model is deduced[25] from the standard MHD equations by substituting $\mathbf{B} = \mathbf{B}_\phi + \mathbf{B_p} = F_0 \nabla \phi + \nabla \psi \times \nabla \phi$ and $\mathbf{v} = \mathbf{v}_{||} + \mathbf{v}_\perp = v_{||}\mathbf{B} + R^2 \nabla \phi \times \nabla u$, therefore assuming constant in the time toroidal magnetic field. Here, $F_0 = B_0 R_0$ is the strength of the magnetic field at the geometric axis $R = R_0$, and ϕ is a toroidal angle. The resulting set of equations describes the evolution of the seven variables, namely, ρ—mass density, T—temperature, ψ—poloidal magnetic flux, $v_{||}$—parallel velocity, u—electric potential, j—toroidal current, and w—vorticity,
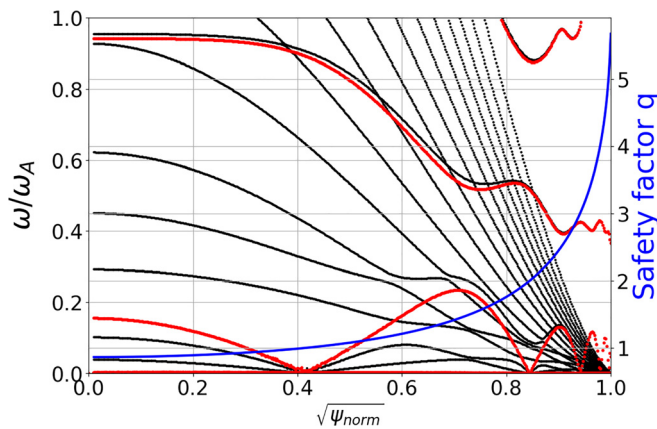

FIG. 12. Alfvén continuum with the inclusion of the sound waves (in black) and without them (in red).
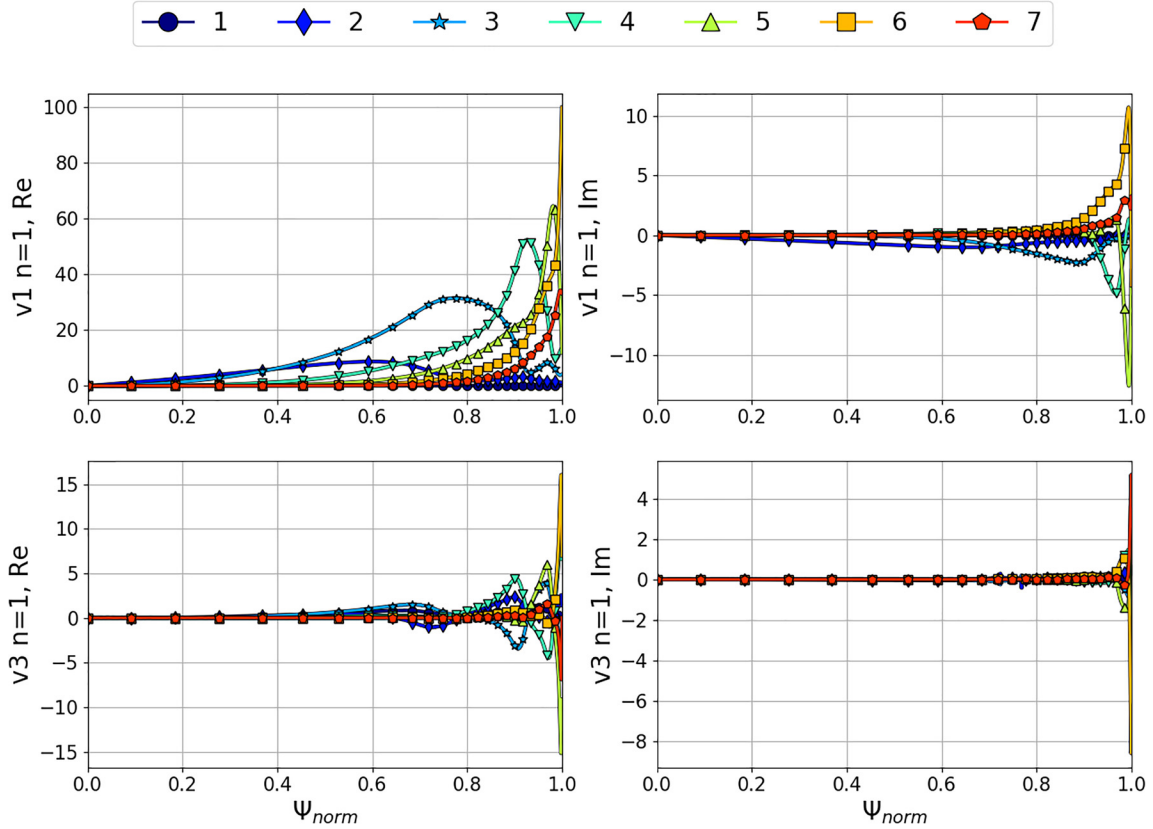
FIG. 13. Mode structure of the $n = 1$ TAE peak for the equilibrium at $t = 54.8$ s without the inclusion of the sound waves. The top row shows the real and imaginary parts of the radial component of the velocity as a function of $s = \sqrt{\psi}$, bottom row—toroidal component of the velocity. Different symbols correspond to the different poloidal harmonics.
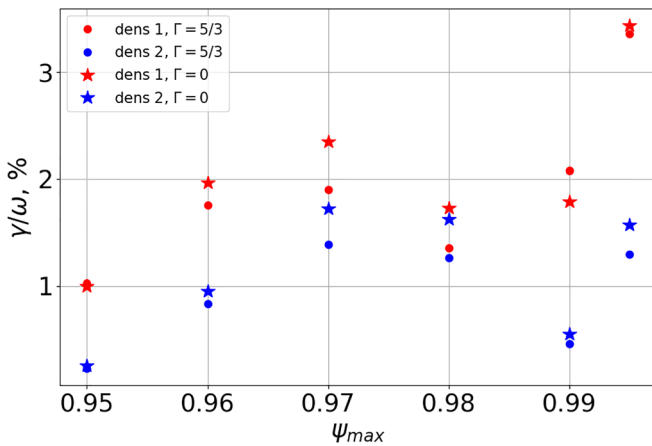
$$\frac{\partial \rho}{\partial t} = -\nabla \cdot (\rho \mathbf{v}) + \nabla (D_\perp \nabla_\perp \rho)$$
$$+ \nabla^2 (D_{\perp hyp} \nabla_\perp^2 \rho),$$

$$\frac{\partial (\rho T)}{\partial t} = -\mathbf{v} \cdot \nabla (\rho T) - (\gamma - 1) \rho T \nabla \cdot \mathbf{v}$$
$$+ \nabla (\kappa_\perp \nabla_\perp T) + \nabla^2 \cdot (\kappa_{\perp hyp} \nabla_\perp^2 T),$$

$$\frac{\partial \psi}{\partial t} = \eta j + R[\psi, u] - F_0 \frac{\partial u}{\partial \phi},$$

$$\rho B^2 \frac{\partial v_\parallel}{\partial t} + \rho v_\parallel \frac{\nabla \psi}{R^2} \frac{\partial \nabla \psi}{\partial t} = -\rho |B|^2 [u, v_\parallel] - \frac{1}{2} \rho v_\parallel [u, B^2]$$
$$- \rho \frac{F_0}{2R^2} \partial_3 \left(v_\parallel^2 B^2 \right)$$
$$+ \frac{1}{2} \rho \left[\psi, v_\parallel^2 |B|^2 \right] - \frac{F_0}{R^2} \partial_3 p - \frac{1}{R} [p, \psi],$$

$$R \nabla \cdot \left[R^2 \rho \nabla_\perp \left(\frac{\partial u}{\partial t} \right) \right] = [R^4 \rho w, u] - \frac{1}{2} \left[R^2 \rho, R^2 |\nabla_\perp u|^2 \right]$$
$$- [R^2, p] + [\psi, j] - \frac{F_0}{R} \frac{\partial j}{\partial \psi} + \mu R \nabla^2 w,$$

$$w = \nabla \cdot \nabla_{pol} u,$$

$$j = \Delta^* \psi = R^2 \nabla \cdot \left(\frac{1}{R^2} \nabla_{pol} \psi \right).$$

FIG. 14. Damping rates as a function of ψ_{max} for the two modified density profiles as illustrated in Fig. 6 and with ($\Gamma = 5/3$) or without ($\Gamma = 0$) the inclusion of the sound waves.
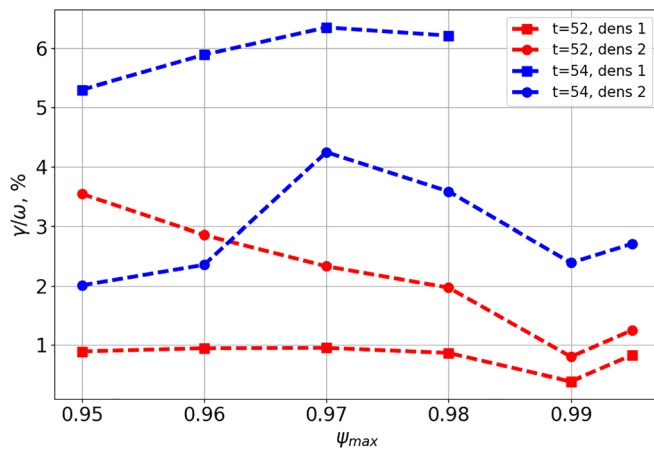
FIG. 15. Damping rates as a function of ψ_{max} for the first TAE peak with the lower frequency.

Here, the $[A, B] = e_\phi \cdot \nabla A \times \nabla B$ notation is used to represent the Poisson bracket and $\nabla_{pol} A = \partial_R A e^R + \partial_Z A e^Z$. A temperature-dependent Spitzer-like resistivity has been used in the simulations: $\eta = \eta_0 (T/T_0)^{-3/2}$, with $\eta_0 = 2.6 \times 10^{-9}\ \Omega\,m$. The value of the resistivity was required to be lower than experimental in order to avoid high damping. The value of the viscosity was set to 4×10^{-9} kg/m s, which was chosen such as to facilitate the convergence of the simulations and does not have a significant effect on the value of the resulting damping rate. The hyperdiffusivities $D_{\perp hyp} = 10^{-8} m^4/s$ and $\kappa_{\perp hyp} = 5 \times 10^{-15}$ kg m/s were used in the simulations to improve the numerical stability.

Cubic Bezier finite elements are used for the spatial discretization in the poloidal plane, while a Fourier representation is used in the toroidal direction. The choice of the finite elements in the poloidal plane allows a very flexible discretization with the geometry, including the accurate representation of the X-point. Finite elements are constructed in such a way that they are aligned with the flux surfaces of
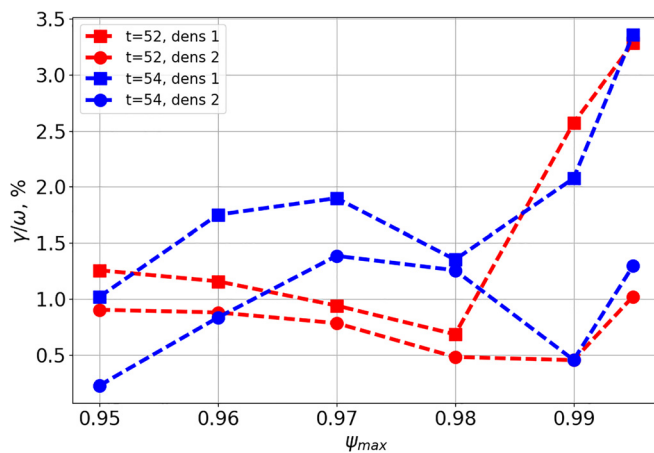

FIG. 16. Damping rates as a function of ψ_{max} for the second TAE peak with the lower frequency.

the initial equilibrium, which allows us to accurately represent the fast parallel transport in the SOL. The time discretization uses the implicit Crank-Nicolson scheme such that the time step necessary for simulations is not restricted by the grid size. The simulations were performed with a time step of $\delta t = 0.5/\sqrt{\mu_0 \rho_0}$ s, which is sufficiently small to resolve the typical TAE frequencies (up to 200 kHz).

The JOREK code is coupled with the STARWALL code, which allows us to include active coils,[26] enabling the simulation of the excitation of TAE modes with an external antenna in full X-point geometry, including the scrape-off layer. The JOREK domain includes the main plasma and the SOL. In the JOREK-STARWALL code, the JOREK domain is surrounded by a vacuum and a resistive wall. As for the CASTOR code, the antenna is situated in the vacuum, and the free-boundary conditions, i.e., continuity of the magnetic field, are used. The magnetic field boundary conditions are calculated by the STARWALL code once before a JOREK simulation for a given plasma and wall geometry. The resulting so-called response matrices are used in JOREK for the magnetic boundary conditions and the time evolution of induced currents in the resistive wall. Here, the resistive wall is modeled on the JET vacuum vessel (see Fig. 21). The wall resistivity is taken to be $2.5 \times 10^{-1}\ \Omega/m$. On the open field lines, leaving the JOREK domain, the boundary conditions on the density, temperature, and parallel velocity are the so-called divertor sheath boundary conditions: the parallel velocity is set to the local sound speed, the condition on the heat flux links the parallel convected and conducted energy through a sheath transmission factor. The density is flowing out naturally. The potential is set to zero on the boundary. On the parts of the JOREK boundary where it is aligned with the magnetic field, the conditions on the temperature, density, parallel velocity, and electric potential at the boundary of the JOREK domain are such that the perturbations with respect to the initial state are set to zero on the JOREK boundary (i.e., outside the SOL).

Unlike CASTOR, the JOREK code was used in a time dependent mode. The plasma-vacuum-antenna system is evolved in time until a stationary state is obtained. The plasma behaves as a driven oscillator, and therefore the response function will look differently for a resonant and off-resonant cases. An example of such a temporal evolution of the kinetic energy of $n = 1$ mode for a limiter case is illustrated in Fig. 17. Here, the dashed curve in gray corresponds to the resonant case with frequency $f = 114$ kHz, and the solid black curve corresponds to the off-resonant case with $f = 120$ kHz. In this example, it can be seen that plasma behaves as a driven damped harmonic oscillator, with its nonresonant response initially growing, but eventually settling down to a steady pattern. Contrarily, its resonant response amplitude grows monotonically until it reaches its final value. The time needed for the steady solution to be reached is inversely proportional to the damping present in the system. The typical simulation time therefore depends on the chosen resistivity and requires $\approx 10^3$ Alfvén times in this set of simulations.

B. Case setup

In order to isolate a specific effect of the presence of the scrape-off layer (SOL), the initial equilibrium taken from the JET shot #42870 at the moment of time $t = 54.88$ s, which corresponds to the X-point phase of the discharge, was analyzed in two ways. In the first case, the plasma boundary was set at the flux surface $\psi_{norm} = 0.995$, therefore not including the SOL, and in the second case, the whole equilibrium
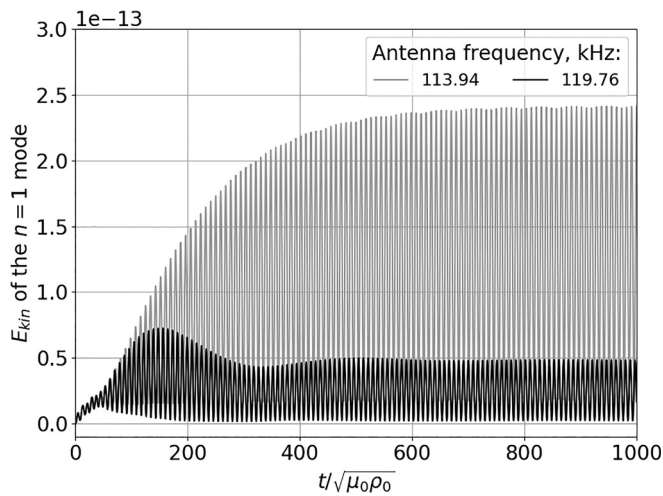
FIG. 17. Temporal evolution of the kinetic energy of $n = 1$ mode for a resonant case with the applied antenna frequency $\omega = 114$ kHz (in dashed gray) and an off-resonant case with frequency with the applied antenna frequency $\omega = 120$ kHz (in black).

with a real X-point and the SOL was taken. The examples of the grids for both cases are illustrated in Fig. 18. The $n = 0$ mode of the equilibrium and initial profiles are kept constant throughout the simulation for both cases, only allowing excitation of the $n = 1$ mode without a

change of the Alfvén continuum. The density profile and, therefore, Alfvén continuum correspond to the ones referred to as the first modified density profile used previously in the studies with the CASTOR code shown in Fig. 5 in red. The scans across the frequency range performed for both cases together with the corresponding CASTOR case are shown in Fig. 19. In the no-SOL case (marked with squares in the figure), two TAE peaks are found, which are split into a main resonance with a frequency $f_1 = 114$ kHz and a smaller peak just at the upper edge of the TAE gap with a frequency $f_2 = 136$ kHz. Since in the no-SOL case, the X-point geometry is not taken into account, the result can be compared to the one produced by the CASTOR code for the same equilibrium. The case analyzed with the CASTOR code is presented in the same figure in a line with star markers with the height of the peak normalized to the same value as the main resonance in the no-SOL JOREK case. The two peaks demonstrate good agreement with the main TAE peak in CASTOR having a slightly higher frequency of $f = 125$ kHz, and a lower damping rate of $\gamma/\omega = 2.1\%$ in CASTOR vs $\gamma/\omega = 4.2\%$ in JOREK. A direct comparison of continua in the two codes is not possible since JOREK is a time-dependent code, and the continuum for it cannot be calculated directly. As both codes are run using the same initial equilibrium and input profiles, and the $n = 0$ mode JOREK is not evolving, one can say with a significant confidence that the Alfvén continua are identical at the beginning of the simulations. A possible explanation for the difference in the resonance frequency between the CASTOR and JOREK results is the presence of the viscosity terms in the JOREK model that are not
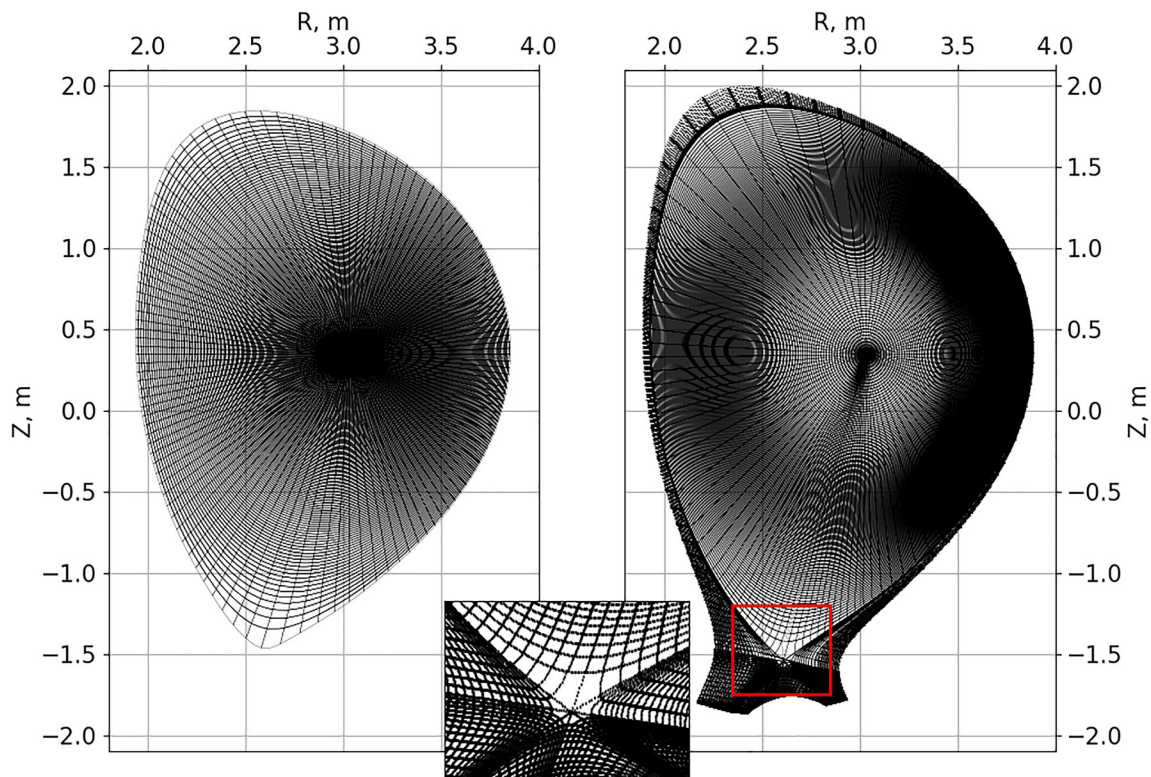

FIG. 18. The grids used in the JOREK simulations in the case without the SOL (left) and with the SOL (right).
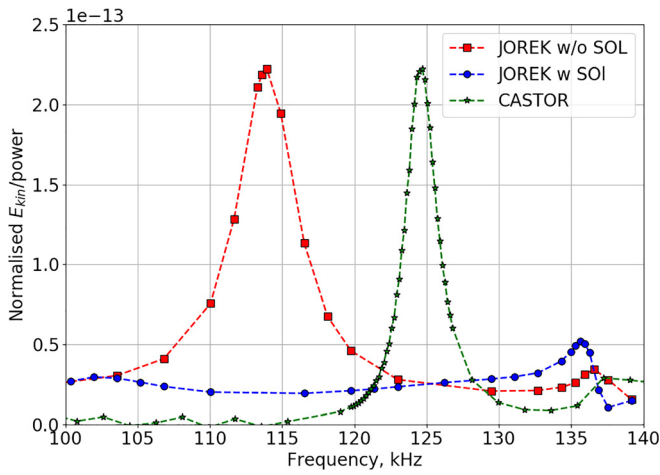
FIG. 19. Frequency scan across the TAE gap for an equilibrium at $t = 54.8$ s. In squares—kinetic energy of the $n = 1$ mode in the JOREK simulation without the SOL. In circles—kinetic energy of the $n = 1$ mode in the JOREK simulation with the SOL. In stars—power absorbed by the plasma calculated via the CASTOR code. The height of the peak is normalized to the peak of the JOREK no-SOL case.

included in the CASTOR MHD model. This may lead to a small modification of the frequency of the TAE modes. The peaks in both codes have a similar mode structure illustrated in Fig. 20.

If in the no-SOL case, the strong resonance observed both in the experiment and in the CASTOR code is recovered, it disappears in the case with the SOL and X-point included. The result of the simulation for this case with X-point is illustrated in Fig. 19 in a line with circular markers. As can be seen, only one of the two original resonances remains, namely, the secondary peak at $f_2 = 136$ kHz.

The 2D poloidal mode structures for the no-SOL and SOL cases are shown in Fig. 21. Note that the amplitude of the modes in the figure has different scales. In the case with no SOL included (top row), the first mode exhibits an even mode structure[27] with a maximum amplitude on the low field side, whereas the second mode with a higher frequency is an odd mode, and its amplitude is higher on the high-field side. Comparing the dominant modes in the no-SOL and SOL cases (on the left in Fig. 21, top and bottom, respectively), it is clearly visible that the mode disappears, when the second mode with a higher frequency (on the right in the figure) remains.

As in the case with the CASTOR code, the necessary poloidal resolution has to be used in the simulations to properly resolve the thin resistive layer. The results of the simulations performed with a different poloidal resolution of the grid are shown in Fig. 22, while the
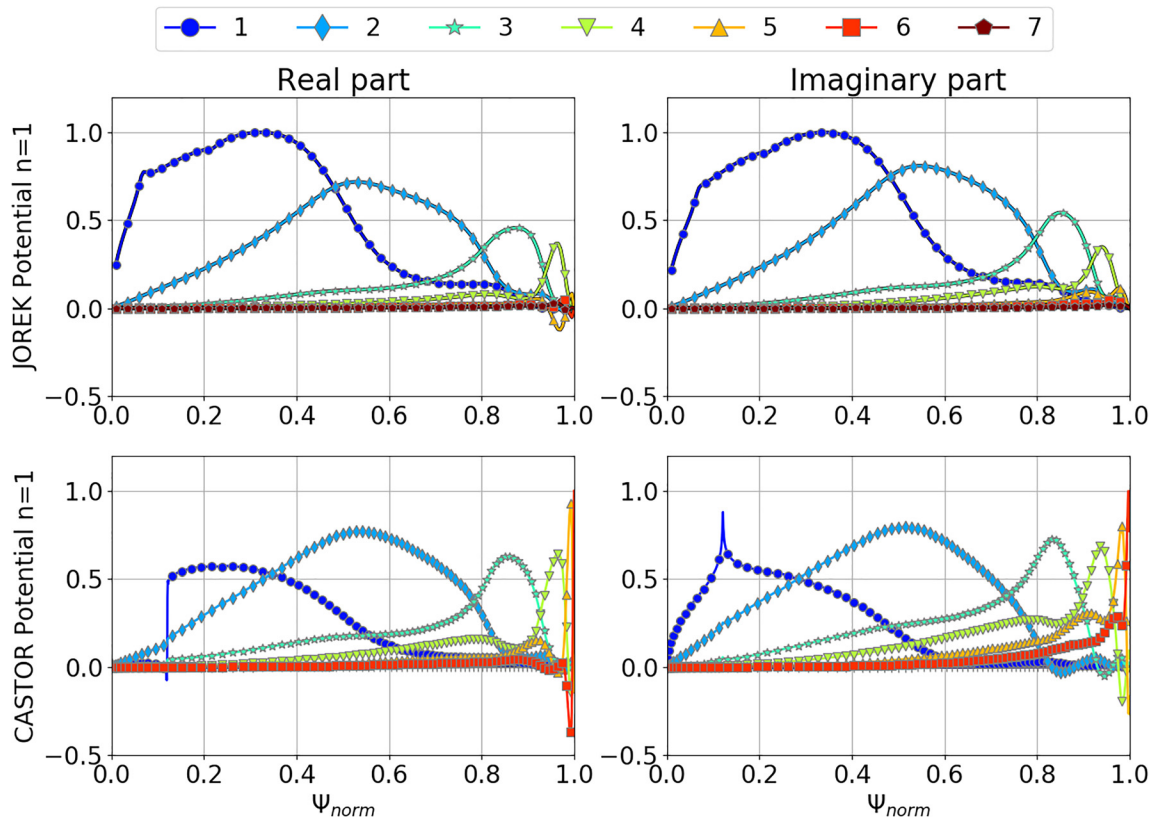

FIG. 20. Mode structures of the main TAE peaks in JOREK (top row) and CASTOR (bottom row) simulations. The real and imaginary parts are presented in the left and the right columns, respectively.
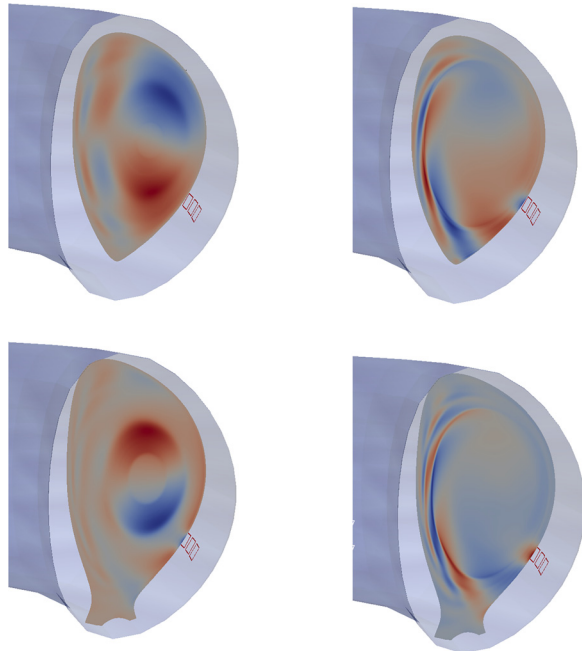
FIG. 21. Poloidal cross sections representing the mode structure of electric potential of the n = 1 mode. The mode structures at the top row clearly demonstrate that these are even (left) and odd (right) modes. The red squares visible slightly below the midplane to the right of the main plasma are the antennas used for the TAE excitation. The mode structure of the TAE with a lower frequency in the case without the inclusion of the SOL. The mode structure of the TAE with a higher frequency in the case without the inclusion of the SOL. The mode structure of the TAE with a lower frequency in the case with the inclusion of the SOL. The mode structure of the TAE with a higher frequency in the case with the inclusion of the SOL.

frequency of the antenna and its position were not changed. A resolution of 101 poloidal points was used in the simulations without the X-point, while the X-point cases required a more accurate grid with 151 points.
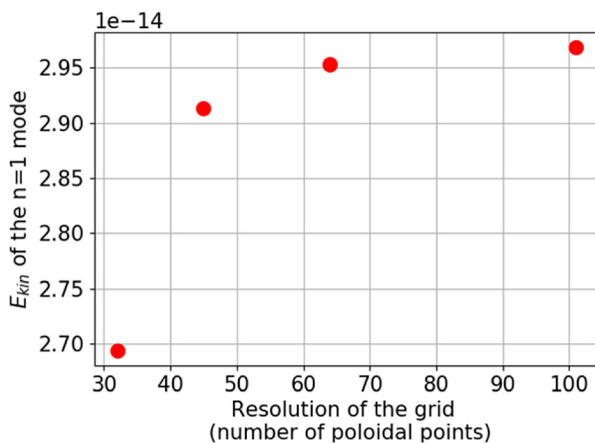

FIG. 22. Dependence of the kinetic energy of the n = 1 mode on the poloidal resolution of the grid.
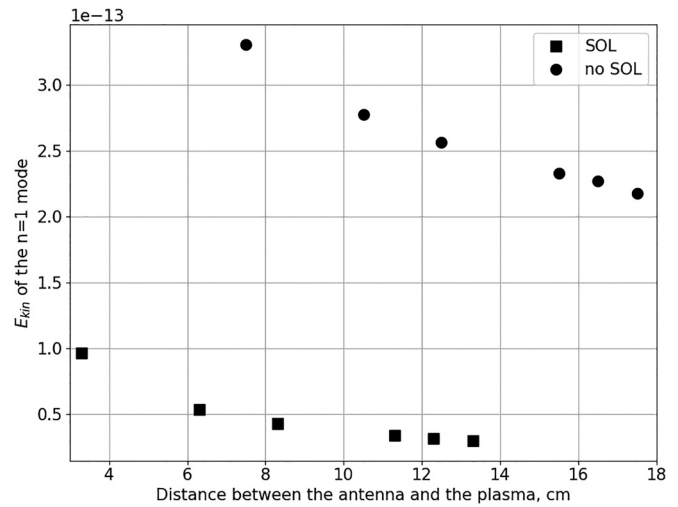

FIG. 23. Dependence of the kinetic energy of n = 1 mode on the distance between the antenna and the plasma.

C. Antenna position

The effect of the distance between the antenna and the plasma could influence the identification of the mode. A scan of the antenna position with regard to the plasma boundary, i.e., the last surface taken into account, was performed while keeping the antenna shape and frequency of the oscillation constant. Note that in both cases, the antenna remains outside of the JOREK grid. The results of the scan for both SOL and no-SOL cases are illustrated in Fig. 23. In both cases, the amplitude of the mode has significantly increased (by more than 50% in the SOL case and by ∼30% in the no-SOL case) with the antenna getting closer to the plasma boundary.
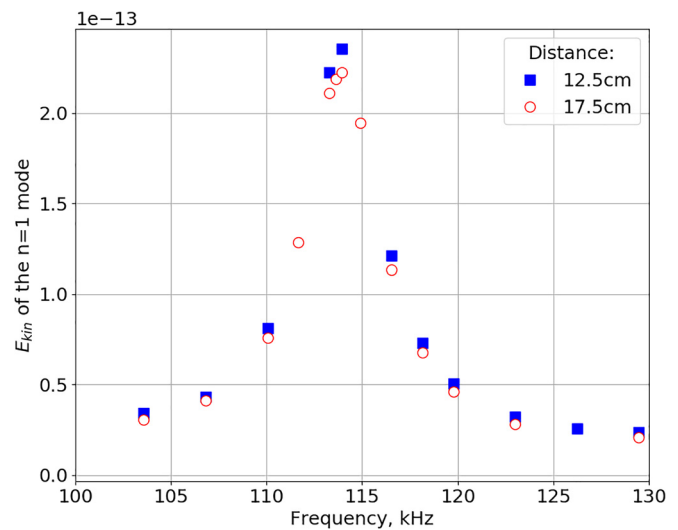

FIG. 24. Dependence of the kinetic energy of n = 1 mode on the applied frequency of the antenna for the no-SOL case with two different antenna positions: 12.5 cm and 17.5 cm away from the plasma boundary.
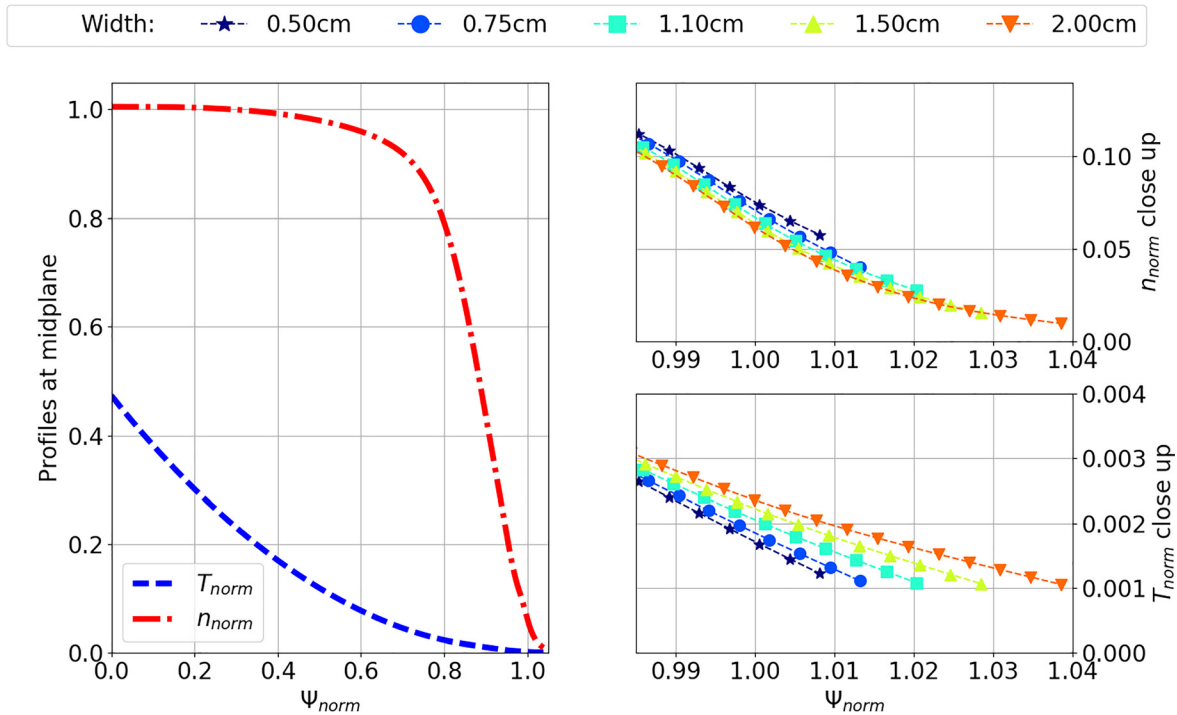
FIG. 25. Left: Midplane density (dash-dotted line) and temperature (dashed line) profiles. Right: density (top) and temperature (bottom) profiles in the near-SOL and SOL-regions for different midplane SOL widths.

For two different antenna positions, the frequency scans were performed, with results presented in Fig. 24. As expected, the damping rate does not depend on the antenna position. However, moving of the antenna closer only influences the amplitude of the mode, therefore complicating the excitation and consecutive identification of the mode.
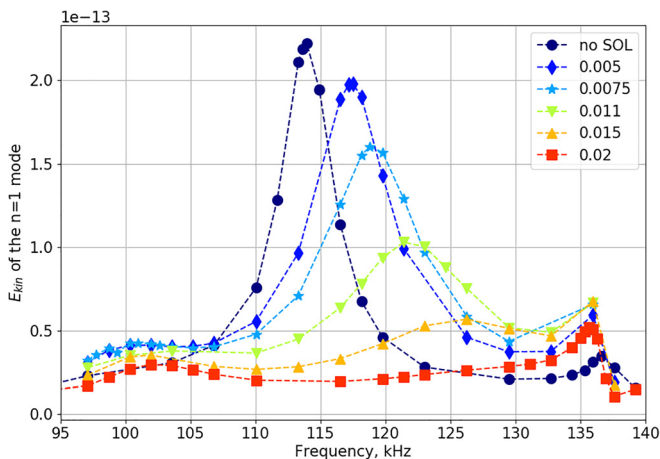

FIG. 26. Kinetic energy of the n = 1 mode as a function of the applied frequency for the different midplane SOL widths. It can be seen in the figure how the main TAE peak located at f = 113 kHz in the no-SOL case gradually decreases with the increase in the SOL width until eventually it cannot be distinguished.

D. Influence of the SOL width

A possible explanation of the increased damping in the X-point phase of the discharge is the existence of the SOL. A set of simulations with the SOL width being varied from 0 cm (corresponding to the case of no SOL present) to 2 cm were performed in an attempt to follow the evolution of the TAE mode. Note that the SOL width here denotes the actual physical width of the SOL in the midplane taken into account in the simulations, not the e-folding length. In Fig. 25(left), the midplane temperature and density profiles are illustrated, with close ups on profiles in the SOL region on the right of the figure.

The results of the SOL width scan are presented in Fig. 26. In the figure, the initial response peaks of the kinetic energy of $n = 1$ TAE mode with the SOL width $d_{SOL} = 0$ cm corresponding to the no-SOL case discussed above at $f = 113$ kHz (main peak) and $f = 137$ kHz (secondary peak) are shown in circular markers. While the secondary peak remains at its place with the increase in the SOL width, the main peak is experiencing a strong damping with its amplitude gradually decreasing with the increase in the SOL width. The related mode structures corresponding to the main peak are shown in Fig. 27, with the mode amplitude slowly vanishing as the SOL width increases.

A possible explanation of the increased damping in the SOL is the existence of an Alfvén continuum on the line-tied open field lines in analogy to what was proven to exist in Ref. 28 for coronal loops, which could cause the continuum damping of the mode in the SOL.

If the theory applies to the tokamak case, one would expect a sudden change in the damping rate with the increase in the SOL width once the resonant surface is included in the SOL. To check this theory,
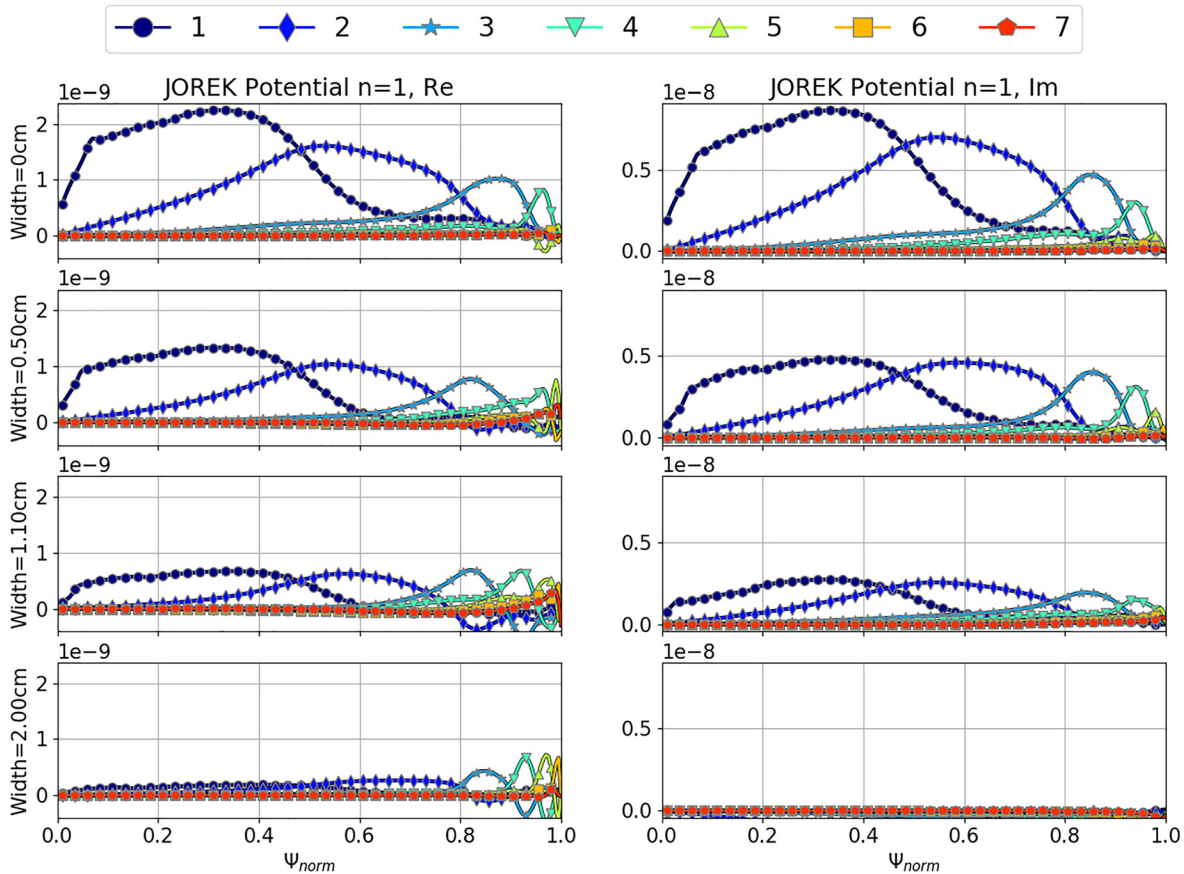
FIG. 27. Radial structure of the real (left) and imaginary (right) parts of $n = 1$ potential of the primary TAE peak for different midplane SOL widths. Different symbols correspond to the different poloidal harmonics.

the damping rates can be calculated knowing the peak width as was done in Sec. II, and the results are shown in Fig. 28 (bottom) with the amplitude of the main peak evolution (top). It can be denoted from the figure that the damping increment is a smooth function, which disagrees with the suggestion of the existence of the continuum. Therefore, the main cause of the increased damping coming from the SOL region is believed to be a wave cut-off by the SOL with the short fieldline lengths, but this assumption requires further investigation.

IV. CONCLUSIONS

This paper discusses the effect of the disappearance of the TAE mode peaks occurring with the transition from the limiter phase of the discharge to the X-point phase observed experimentally on JET with the saddle coils used as an external TAE antenna and made an attempt to identify the reasons causing this effect.

In the first part of this paper, the influence of the near-SOL layer from the plasma core side with the use of the linear resistive MHD code CASTOR was studied. The results for two different magnetic configurations and two density profiles chosen such that the gap in the Alfvén continuum is kept open to exclude the continuum damping were obtained. In both cases, two TAE resonances located in the open
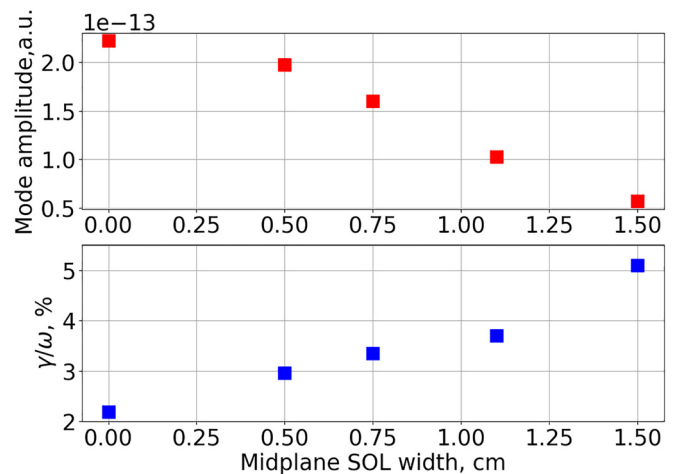

FIG. 28. Mode amplitude (top) and damping rate (bottom) as a function of the midplane SOL width. The gradual decrease of both the mode amplitude and the damping rate refutes the assumption of the continuum damping on the open field lines as was illustrated for the coronal loops in Ref. 27.

gap were identified, with damping rates of up to 6% for the first minor peak with lower frequency and of 1–3% for a major peak with higher frequency, which are comparable values with the typical experimental results. The TAE with a lower frequency does not exhibit any specific trend with the domain boundary approaching the separatrix. However, the main TAE peak with the higher frequency in all four cases has a trend of the increased damping coming from the near-SOL region.

The second part of this paper was concentrated around a study of the presence of the separatrix and the SOL on the mode behavior in the nonlinear resistive MHD code JOREK coupled to the STARWALL code, allowing us to directly model the experiments with the sweeping antenna signal. Including the X-point and SOL, the results similar to the ones obtained before in the experiment were recovered, namely, the absence of the detectable mode in the X-point case. The influence of the distance between the plasma and the antenna and the damping in the SOL were addressed. The antenna positioning had affected the TAE amplitude with the move from 10 cm to 1 cm away from the boundary causing the mode amplitude increase by 30%. It was shown that the dominant effect on the damping of the original mode observed in the limiter configuration is caused by the change of the SOL width.

ACKNOWLEDGMENTS

REFERENCES

[1] C. Cheng, L. Chen, and M. Chance, Ann. Phys. **161**, 21 (1985).

[2] A. Fasoli, D. Testa, S. Sharapov, H. L. Berk, B. Breizman, A. Gondhalekar, R. F. Heeter, M. Mantsinen, and Contributors to the EFDA-JET Workprogramme. Plasma Phys. Controlled Fusion **44**, B159 (2002).

[3] A. Fasoli, D. Borba, G. Bosia, D. J. Campbell, J. A. Dobbing, C. Gormezano, J. Jacquinot, P. Lavanchy, J. B. Lister, P. Marmillod et al., Phys. Rev. Lett. **75**, 645 (1995).

[4] J. Moret, CRPP Laboratory Report LRP No. 498/94 (1994).

[5] A. Fasoli, D. Testa, T. Panis, A. Klein, J. Snipes, J. Sears, M. Gryaznevich, R. Martin, S. Pinches et al., Plasma Phys. Controlled Fusion **52**, 075015 (2010).

[6] A. Jaun, A. Fasoli, and W. W. Heidbrink, Phys. Plasmas **5**, 2952 (1998).

[7] D. Testa, A. Fasoli et al., Nucl. Fusion **41**, 809 (2001).

[8] J. Snipes, N. Basse, C. Boswell, E. Edlund, A. Fasoli, N. Gorelenkov, R. Granetz, L. Lin, Y. Lin, R. Parker et al., Phys. Plasmas **12**, 056102 (2005).

[9] D. Testa, C. Boswell, and A. Fasoli, Nucl. fusion **45**, 907 (2005).

[10] W. Kerner, J. Goedbloed, G. Huysmans, S. Poedts, and E. Schwarz, J. Comput. Phys. **142**, 271 (1998).

[11] G. Huysmans and O. Czarny, Nucl. Fusion **47**, 659 (2007).

[12] D. O'Brien, L. Lao, E. Solano, M. Garribba, T. Taylor, J. Cordey, and J. Ellis, Nucl. Fusion **32**, 1351 (1992).

[13] S. Poedts and E. Schwartz, J. Comput. Phys. **105**, 165 (1993).

[14] J. Goedbloed, Phys. Fluids **18**, 1258 (1975).

[15] Y.-P. Pao, Nucl. Fusion **15**, 631 (1975).

[16] H. Grad, Phys. Today **22**(12), 34 (1969).

[17] L. Chen and A. Hasegawa, Phys. Fluids **17**, 1399 (1974).

[18] D. Borba, K. S. Riedel, W. Kerner, G. T. A. Huysmans, M. Ottaviani, and P. J. Schmid, Phys. Plasmas **1**, 3151 (1994).

[19] G. Huysmans, W. Kerner, D. Borba, H. Holties, and J. Goedbloed, Phys. Plasmas **2**, 1605 (1995).

[20] M. N. Rosenbluth, H. L. Berk, J. W. Van Dam, and D. M. Lindberg, Phys. Fluids B **4**, 2189 (1992).

[21] F. Zonca and L. Chen, Phys. Rev. Lett. **68**, 592 (1992).

[22] M. Li, B. Breizman, L. Zheng, and E. Y. Chen, New J. Phys. **17**, 125001 (2015).

[23] S. Poedts, W. Kerner, J. Goedbloed, B. Keegan, G. Huysmans, and E. Schwarz, Plasma Phys. Controlled Fusion **34**, 1397 (1992).

[24] M. V. Falessi, N. Carlevaro, V. Fusco, G. Vlad, and F. Zonca, Phys. Plasmas **26**, 082502 (2019).

[25] H. Strauss, J. Plasma Phys. **57**, 83 (1997).

[26] M. Hölzl, P. Merkel, G. T. A. Huysmans, E. Nardon, E. Strumberger, R. McAdams, I. Chapman, S. Günter, and K. Lackner, J. Phys.: Conf. Ser. **401**, 012010 (2012).

[27] H. L. Berk, J. Van Dam, D. Borba, J. Candy, G. Huysmans, and S. Sharapov, Phys. Plasmas **2**, 3401 (1995).

[28] G. Halberstadt and J. Goedbloed, Astron. Astrophys. **280**, 647 (1993).